Version of Record: https://www.sciencedirect.com/science/article/pii/S002223132031632X
Manuscript_58319d5235e8c53fbd3930e38d229871

Characterization of the Ce,Pr:LuAG Phosphor for Co-doped Aerosol Phosphor Thermometry

Joshua M. Herzog, Dustin Witkowski, David A. Rothamer

University of Wisconsin-Madison, 1500 Engineering Dr., Madison, WI 53706

Abstract

The Ce,Pr:LuAG phosphor is investigated for use in co-doped aerosol phosphor thermometry (APT). The phosphor was characterized by measuring the emission intensity for each ion as a function of excitation laser fluence and temperature. A simplified three-level model was used to interpret and fit the data. The phosphor was then used for co-doped APT temperature-imaging experiments performed in a heated air jet up to a maximum temperature of 694 K. The three-level model fit was used to analyze sources of bias in the imaging measurements. Both ions' emission intensities show a nonlinear dependence on excitation fluence that can potentially be explained by temperature-dependent ground- and excited-state absorption processes included in the three-level model. Single-shot temperature precision from the temperature-imaging experiments was measured to be 22, 23, and 32 K for mean temperatures of 497, 603, and 694 K, respectively, at a spatial resolution of ~1.12 lp/mm and average fluence of 33 mJ/cm^2. The results extend the measurement range for co-doped APT to at least 700 K. The findings also provide a simple model for phosphor signal non-linearity with excitation fluence for low activator ion concentrations, and provide a method for estimating temperature bias from several sources including laser fluence.

Keywords: Aerosol phosphor thermometry, Thermographic phosphors, excited-state absorption, co-doped phosphor

1. Introduction

Accurate spatially- and temporally-resolved temperature measurements are needed to further our understanding of complex processes occurring in reacting environments, such as the ignition of high-pressure turbulent fuel jets in engines. Aerosol phosphor thermometry (APT) is a promising technique for these applications. It uses the temperature-sensitive emission properties of phosphor particles seeded into the flow to perform minimally-intrusive single-shot measurements of gas temperature fields. When combined with Mie scattering measurements of the seeded particles, the technique readily integrates with particle image velocimetry (PIV) for thermographic PIV measurements [1]. Phosphors are often composed of rare-earth ions doped into solid chemically-inert ceramic hosts, making APT insensitive to pressure and gas composition in most cases. Furthermore, a wide range of phosphor host-ion combinations are possible, allowing tailoring of material composition for a given experimental condition.

Various phosphor compositions and techniques have been explored recently for gas temperature measurements including ZnO [2, 3, 4], Pr:YAG [5], Ce:LuAG [6], Ce,Pr:YAG [7], and Eu:BAM [8, 9]. A significant amount of work has also focused on new methods to reduce measurement bias, *e.g.*, through structured illumination methods largely with the Eu:BAM phosphor [10, 11]. For a recent review of APT, refer to [12].

To date, most APT measurements of gas temperature have used the spectral luminescence intensity ratio (SLIR) approach [12]. This is in contrast to surface temperature measurements that often use the luminescence lifetime to determine temperatures [13]. The SLIR method captures luminescence within two wavelength bands and relates the emission intensity ratio to temperature, with temperature sensitivity resulting from changing emission bandshape. To optimize temperature precision, a trade-off must be made between collection bandwidth (*i.e.*, signal) and temperature sensitivity. The technique also suffers from decreased signal due to thermal quenching, and decreasing sensitivity with increasing temperature, limiting its utility at combustion-relevant temperatures.

Recently, a novel APT strategy comparing the emission intensity of two ions doped into a single host (co-doped APT) was reported and demonstrated for temperatures up to 450 K using cerium and praseodymium doped into yttrium aluminum garnet (Ce,Pr:YAG) [14]. Since the co-doped APT method collects the entire emission band of each ion, there is no trade-off between temperature sensitivity and luminescence signal. Instead, temperature sensitivity is a result of thermal luminescence quenching. Quenching behavior is intrinsic to the phosphor, such that the temperature sensitivity is not strongly related to the experimental design, *i.e.*, selection of filter pass bands. Additionally, the entire emission band may be collected for each ion, maximizing the collected signal. Finally, phosphors can be 'engineered' for specific temperature ranges through selection of the ion-host combination [7].

This work reports on a new phosphor composition for co-doped APT, trivalent cerium and praseodymium (Ce^{3+} and Pr^{3+}) doped into a lutetium aluminum garnet host

(Ce,Pr:LuAG), to extend the temperature range of the co-doped APT technique up to 700 K. Background is provided on Ce,Pr:LuAG phosphor photophysics, including estimated emission lifetimes and details of the electronic structure. Experimental results for emission intensity of each ion as a function of laser-fluence and temperature are presented. A three-level population model is derived and used to characterize and interpret the observed emission properties. Finally, results from a temperature imaging experiment are presented and temperature precision of the technique is assessed. The primary goal of this paper is to provide a detailed characterization of the Ce,Pr:LuAG phosphor and of its APT diagnostic performance, including temperature precision and bias estimates.

2. Background

For co-doped APT, luminescence emission is collected in two different wavelength bands following excitation by the laser pulse. Each band corresponds to emission from one of the two ions doped into the phosphor host material. The dopant ions are selected to have significantly different quenching temperatures. As will be discussed in more detail, for Ce,Pr:LuAG the Pr^{3+} emission begins quenching at a lower temperature than the Ce^{3+} emission, such that as the Pr^{3+} emission decreases with increasing temperature, the Ce^{3+} emission remains relatively unchanged. This causes the co-doped signal ratio

$$R = \frac{S_{Ce}}{S_{Pr}}, \tag{1}$$

where S_{Ce} and S_{Pr} are the Ce^{3+} and Pr^{3+} signal intensities, to increase rapidly with temperature up to the point where Ce^{3+} emission begins to be significantly thermally quenched.

Co-doped APT performance strongly depends on the quenching properties of the selected phosphor. To first order, the temperature precision, as represented by the precision index s_T (sample temperature standard deviation), of a ratiometric thermometry technique can be expressed as

$$s_T^2 \approx \left(\frac{\partial T}{\partial R}\right)^2 s_R^2 = \left(\frac{s_R/R}{\xi_T}\right)^2 \tag{2}$$

where the ratio (s_R) precision index is the sample distribution standard deviation for the ratio. The fractional temperature sensitivity (ξ_T) is given by

$$\xi_T = \frac{1}{R}\frac{\partial R}{\partial T} = \frac{1}{S_{Ce}}\frac{\partial S_{Ce}}{\partial T} - \frac{1}{S_{Pr}}\frac{\partial S_{Pr}}{\partial T}. \tag{3}$$

The temperature precision index is thus minimized when signal intensity and temperature sensitivity are maximized. Since sensitivity and signal intensity for co-doped APT are determined largely by quenching, an understanding of the phosphor photophysics determining these quantities is necessary for designing and characterizing phosphors.

Figure 1 displays a combined electronic structure and configurational-coordinate diagram for Ce,Pr:LuAG. Positioning of the $4f$ and $4f5d$ states relative to the valence band (VB) and conduction band (CB) was calculated using the work of Dorenbos [15]. Harmonic vibrational structure is superimposed based on experimental data using the approach of Witkowski and Rothamer [16] under the assumption that there is no interaction between the Pr^{3+} and Ce^{3+} ions. Energies are measured relative to the valence band maximum (VBM). The relative location of energy eigenstates, and emission and absorption transitions, can be observed for each ion. In particular, the right-hand side of the diagram shows measured emission spectra for each ion from the co-doped phosphor (from [7]), shifted such that spectral features are aligned with the corresponding ground state $4f$ energy level.

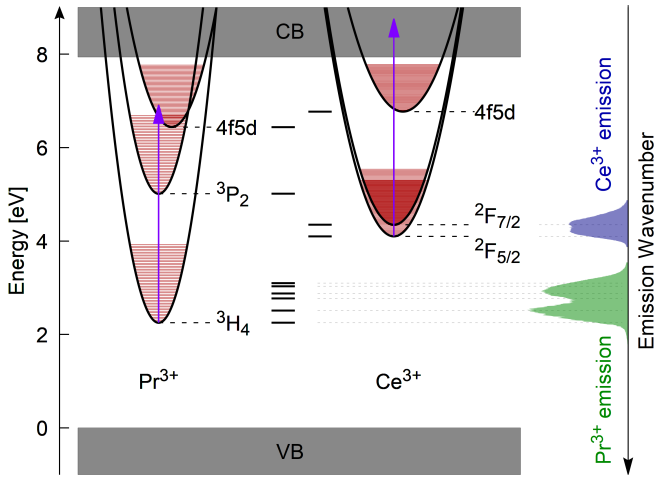

Figure 1: Electronic structure diagram for Ce,Pr:LuAG with the Pr^{3+} ion on the left and the Ce^{3+} ion on the right. The black curves indicate the electronic energy levels (with parabolas explicitly representing the harmonic oscillator potential energy surface) and vibrational energy levels represented by horizontal red lines. Data used to generate this diagram is from [16]. The vertical purple arrows indicate the 266 nm excitation from the lowest-lying $4f$ state for each ion. The emission spectra, from [7], are shown for each ion on the right.

The configurational-coordinate diagram in Figure 1 can also be used to identify potential thermal quenching processes. Excitation of a $4f$ electron to a $5d$ orbital is generally followed by rapid nonradiative relaxation to the lowest excited state for the $5d$ electron as a result of lattice vibration excitation [17]. Thermal quenching of $5d$ emission can then occur through several mechanisms, with each mechanism characterized by an energy gap. Nonradiative relaxation of the electron from d to f orbitals occurs through thermally-activated intersystem crossing, with a rate that is dependent on the energy difference between the bottom of the lowest $5d$ potential and the crossing point between the $5d$ potential and closest $4f$ potential. Thermal activation can also promote the electron to the conduction band with a rate that is dependent on the energy difference between the bottom of the lowest $5d$ energy level and the bottom of the conduction band. Promotion to the conduction band generally results in eventual nonradiative (or radiative) deactivation of the electron through a different path [18].

It has been shown previously that quenching occurs primarily through the mechanism with the smallest characteristic energy, and that this energy gap is approximately linearly related to the temperature at which quenching begins [19]. Referring

to Figure 1, the apparent dominant quenching mechanism for Pr^{3+} can be readily identified as intersystem crossing between the $5d$ excited state and the highest-lying $4f$ triplet state ($^3P_2$). This appears in the diagram as an intersection in the potential energy surfaces of these two electronic levels (~7 eV from the VBM). In contrast, Ce^{3+} quenching appears to result from electron transfer to the conduction band. This is evident in the diagram from the close proximity of the Ce^{3+} $5d$ level to the conduction band relative to the Ce^{3+} intersystem crossing point (over 8 eV from the VBM). The two ions are expected to quench at different temperatures because the respective energy gaps are significantly different in magnitude. The energy gaps just mentioned are larger in Ce,Pr:LuAG than those in the previously studied Ce,Pr:YAG [16], which suggests potential to measure higher temperatures for this phosphor composition relative to Ce,Pr:YAG.

The stated thermal quenching trends can be confirmed with phosphor lifetime measurements. Lifetimes for Ce^{3+} and Pr^{3+} are presented in Figure 2 using data from [16]. The lifetime data presented are for singly-doped Ce:LuAG and Pr:LuAG. While higher doping concentrations can potentially change the lifetime of the emission [20], the effect here is expected to be secondary based on estimates of the resonant dipole-dipole energy transfer between Ce^{3+} and Pr^{3+} for the co-doped phosphor. The lifetime results in Figure 2 show the expected trends based on the earlier thermal quenching discussion. Quenching in Pr^{3+} begins at much lower temperatures relative to Ce^{3+}, and the quenching temperatures for both ions in LuAG (700 K for Ce^{3+}, and 430 K for Pr^{3+} based on a 10% reduction in lifetime) are higher than previously observed in YAG.

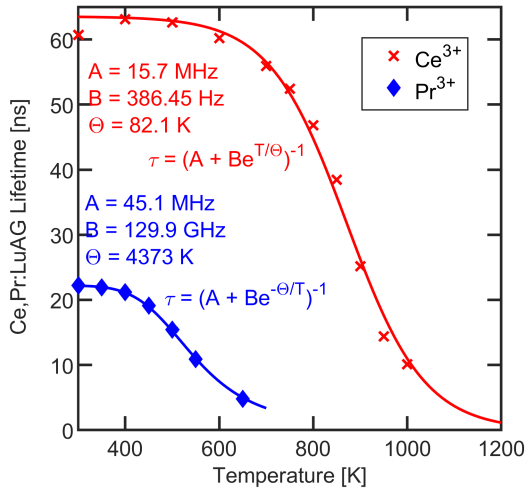

Figure 2: Experimental flurescence lifetimes of Ce:LuAG and Pr:LuAG taken as a function of temperature, with data from [16].

From this background discussion, there are several interesting features that suggest Ce,Pr:LuAG is a promising candidate for co-doped APT. Ce^{3+} and Pr^{3+} have different quenching temperatures, and the values of both are larger in LuAG relative to YAG. The larger energy gaps in LuAG imply that Ce,Pr:LuAG should extend the high temperature-limit for the co-doped APT technique relative to Ce,Pr:YAG. Further, since Pr^{3+} quenches at a lower temperature, high sensitivity is expected from Pr^{3+} emission intensity temperature dependence up to the onset of Ce^{3+} quenching. Finally, since the $4f \leftrightarrow 5d$ electronic energy gap differs significantly between Ce^{3+} and Pr^{3+}, the ions emit in distinct wavelength regions and the entire emission of each ion can be collected without interference.

3. Experimental methods

Imaging of phosphor aerosols in a jet of moderate diameter at low particle concentrations provides an environment where multiple scattering and radiative trapping are limited, such that the emission properties of the phosphor can be directly studied. In contrast, measurements of bulk phosphor powder in a furnace gives valuable information but can be impacted significantly by the mentioned effects [21]. To isolate the photophysics of Ce,Pr:LuAG, measurements of phosphor particle luminescence and elastic light scattering were performed in a seeded air jet as a function of temperature, seeding density, and laser fluence. Temperature imaging experiments were performed using the same experimental setup. Data for phosphor photophysics characterization were acquired for temperatures ranging from 300 to 700 K in 100 K increments. At each temperature, measurements were taken varying laser fluence from ~5 to 35 mJ/cm^2 (on average) using 266-nm pulsed laser light for excitation. The temperature imaging experiments reported here were performed for a single fluence (35 mJ/cm^2) at varying jet exit temperatures ranging from room temperature to approximately 700 K.

3.1. Experimental setup

The experimental layout for signal collection is shown in Figure 3. Luminescence emitted by the phosphor particles was collected on two cameras, situated on either side of the heated air jet, with appropriate filters to image Pr^{3+} emission on one and Ce^{3+} emission on the other. A beamsplitter and a third camera were used to simultaneously measure the 90° elastically scattered laser light which was used to determine the local particle seeding concentration. The Ce,Pr:LuAG powder (Phosphor Technology, ZMK59C/FF-X) was manufactured with a target particle diameter of 1 μm, and a doping concentration of 0.5% for each ion. The particle size distribution was measured by the manufacturer, and derived properties used in this study are listed in Table 1.

The Pr^{3+} emission from Ce,Pr:LuAG particles in the jet was imaged onto an intensified CCD camera (ICCD) (Princeton Instruments, PI-MAX4 1024i-HB-FG-18-P46) with a Gen. III HBf intensifier. The Pr^{3+} camera was outfitted with a 45-mm focal length f/1.8 UV lens (Sodern Cerco, 2073). Two UV rejection filters (Schott Glass, WG295 (3-mm thick); and Semrock Inc., FF01-267) and a 450-nm shortpass filter (Melles Griot O3SWP604) were used to limit the collection band to 290-450 nm.

The Ce^{3+} camera and the camera capturing elastically scattered laser light (scattering camera) were placed on the opposite side of the laser sheet from the Pr^{3+} camera. A 347-nm

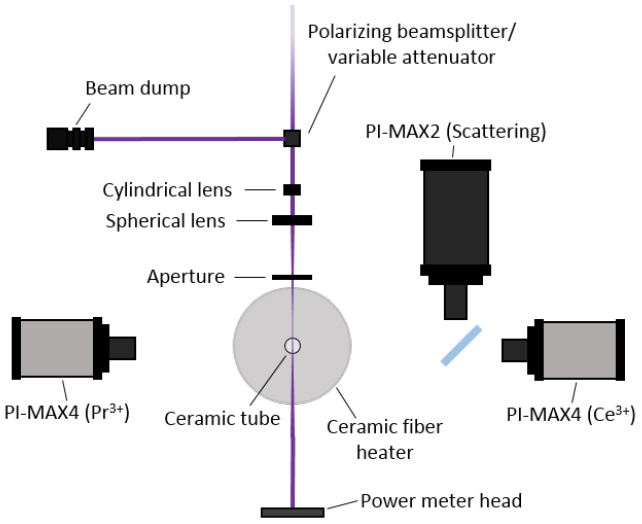

Figure 3: Experimental setup diagram for seeded jet characterization and validation experiments.

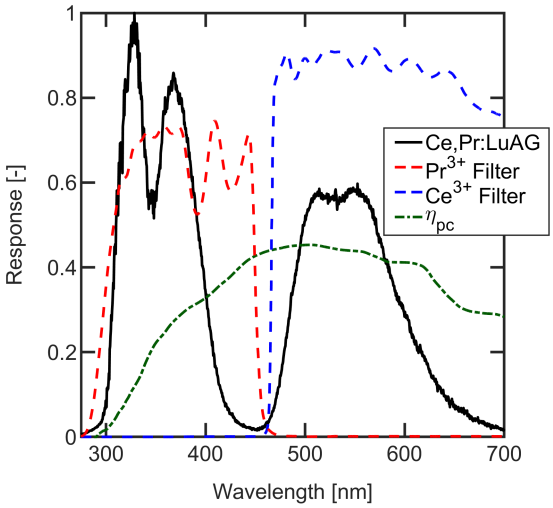

Figure 4: Room temperature emission spectrum (solid black curves), with camera collection bands superimposed (dashed curves).

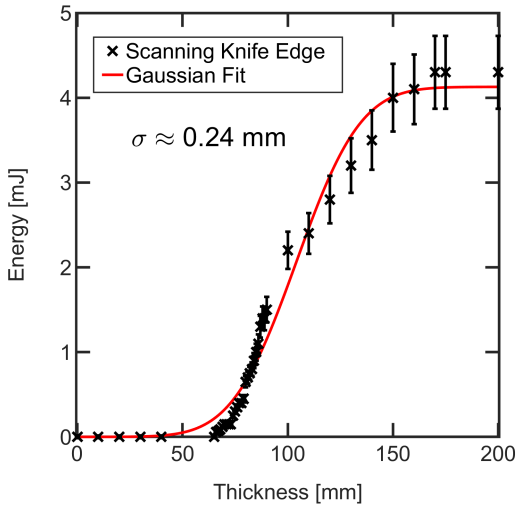

Figure 5: Integrated laser profile based on the scanning knife edge technique with Gaussian fit superimposed.

long-pass dichroic beamsplitter (Semrock Inc., FF347-Di01) was used to reflect elastically scattered laser light to the scattering camera while allowing longer wavelengths to be transmitted to the Ce^{3+} camera. The Ce^{3+} emission was imaged using an ICCD camera identical to that used for imaging Pr^{3+} emission (Princeton Instruments, PI-MAX4 1024i-HB-FG-18-P46). The Ce^{3+} camera was outfitted with an f/1.4 85-mm Nikon Nikkor lens with a 295-nm long-pass filter (Schott Glass WG295, 3 mm thick), used to ensure sufficient rejection of scattered laser light, and a 470-nm long-pass filter (Asahi Spectra ZVL0470) resulting in a collection band from 470 to 750 nm.

A third ICCD camera (Princeton Instruments, PI-MAX2 7489-0022) outfitted with a 105-mm f/4.5 UV Nikon Nikkor lens was used to image the elastically-scattered laser light. A 300-nm shortpass filter (Asahi Spectra, ZUS0300) was used to reject phosphor emission in combination with a 280-nm long-pass filter (Schott Glass WG280 3mm) that was used to limit the elastic scattering intensity to avoid intensifier damage.

The transmission spectra for the Pr^{3+} and Ce^{3+} collection bands, along with room temperature emission spectra, are shown in Figure 4. The Pr^{3+} emission ranges in wavelength from approximately 300 to 450 nm, whereas the Ce^{3+} begins around 450 nm and extends out to about 700 nm. The filter collection bands used effectively isolate the the individual ions' emission to their respective cameras. Spectral response of the Nikon lens has been measured and reported previously in the literature [22], and is included in the collection bands. Spectral response of the Sodern Cerco 45-mm UV lens is unknown, but the manufacturer reports 85% transmission, and this figure is used for the collection band plot.

The 266-nm fourth-harmonic output of a Q-switched, flashlamp-pumped Nd:YAG laser (Ekspla, NL 303D-10) was used to excite the phosphor at a repetition rate of 10 Hz. The laser beam was formed into a 20-mm tall sheet using a -75-mm focal length cylindrical lens, followed by a 200-mm focal length spherical lens. The laser sheet 5-95% thickness was measured to be 0.9 ± 0.1 mm using the scanning knife edge technique at the center of the jet; the integrated profile is shown in Figure 5 with a Gaussian fit superimposed. The peak laser intensity in the sheet was estimated to be approximately 50% larger than the average. The laser sheet is focused at the front edge of the jet to avoid breakdown within the jet. The edges of the laser sheet were clipped to remove the low-intensity tails. Average laser power during the laser pulse is approximately 1 MW for the cases with 6 mJ/pulse laser energy (using the manufacturer specified 6 ns FWHM laser pulse width); this corresponds to the 35 mJ/cm^2 fluence case.

Phosphor particles were seeded into a room temperature compressed air flow using a fluidized bed aerosol generator (TSI, Model 3400A) at an inlet gauge pressure of 240 kPa. The aerosol flowed through a horizontal tube with an inline 6-kW electric heater (Sylvania, 038825), then through a 19-mm ID

Table 1: Parameters used in Mie scattering calculation for Ce,Pr:LuAG

Quantity	Symbol	Value	Units
Volume-weighted radius	$r_{p,V}$	0.52	µm
Area-weighted radius	$r_{p,A}$	0.49	µm
Number-weighted radius	$r_{p,N}$	0.45	µm
Extinction efficiency	$Q_{ext}(r_{p,A})$	2.4	-
Extinction cross-section	σ_{ext}	1.8	µm^2

vertical ceramic tube heated externally by a 1.8-kW annular vacuum-formed ceramic-fiber heater (Thermcraft Inc. Fibercraft, VF180224-V). The total air flow rate was 28.3 slpm. The temperature profile of the jet was measured 20±3 mm above the tube exit using a bare wire type-K thermocouple (0.01" wire dia., 0.021" bead dia.) and thermocouple reader (Omega, Omegaette HH308) with an estimated combined uncertainty of 1%. No corrections are applied to the thermocouple readings. The maximum bias is estimated to be 10 K for the highest temperature cases as a result of conduction and radiation.

3.2. Determination of intensity per particle

The elastic scattering images have been calibrated to number density to provide a quantitative estimate of signal per particle. This procedure uses optical extinction measurements and the Beer-Lambert relation, and has been discussed in detail in previous publications [21, 7]. Although the phosphor particles are non-spherical, Mie theory has been used successfully for characterizing non-spherical particles; particle shape and orientation are expected to have only a small influence on scattering intensity [23]. Mathematically, the particle number density (n_p) is expressed as

$$n_p = -\ln\left(\frac{I}{I_0}\right)\frac{1}{\sigma_{ext}L} \quad (4)$$

where I/I_0 is the measured transmission, σ_{ext} is the extinction cross-section from Mie theory (using the phosphor particle size distribution and index of refraction from [24]), and L is the path length. Parameters used in this calculation were estimated from manufacturer-provided data, and are given in Table 1. The extinction coefficient integrated across the width of the jet for all experiments here is less than 2%. All experiments are performed in the low absorption regime, and laser fluence is approximately constant throughout the jet. Based on the best-fit absorption cross-sections that will be discussed in Section 4.4, elastic scattering dominates the laser extinction throughout the jet. The absorption process accounts for about 0.075% of the attenuation at 300 K at low fluence. Typical extinction coefficients at the seeding densities used here are ~1 m^{-1}, and absorption coefficients are 0.00075 m^{-1}.

The extinction measurements were used to calibrate scattering intensity to absolute number density. Mie scattering images were taken simultaneously with the extinction measurements for a range of seeding densities to determine the relationship between scattering intensity S_{Mie} and number density n_p. It has been shown previously that Mie scattering intensity is linearly proportional to both number density and laser energy [21], and thus number density and scattering intensity are related linearly, $n_p = cS_{Mie}$. The proportionality constant c is determined by linear regression of the Mie scattering intensity and extinction data (please refer to [7] for more information on this procedure).

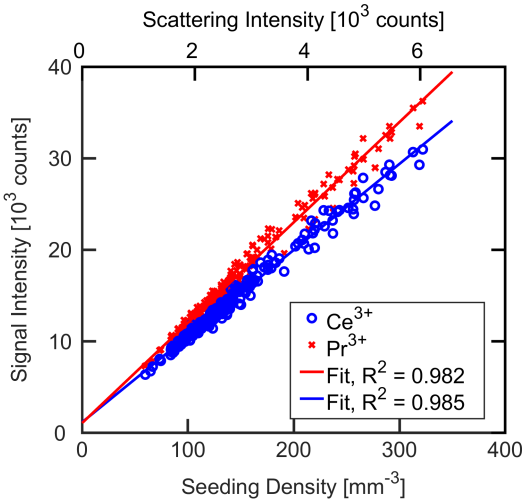

Figure 6: Measured emission intensity for Ce^{3+} (blue) and Pr^{3+} (red) at room temperature and with an average fluence of 33 mJ/cm^2 as a function of scattering intensity (top axis) and seeding density (bottom axis).

To determine number density in the imaging experiments, Mie scattering images were first corrected for background and the average laser sheet energy profile (flatfield correction). The sheet profile was determined from room temperature Mie scattering measurements and verified with measurements using the scanning knife edge technique. Next, using the linear regression from the extinction data, scattering images were converted to number density images by multiplying the scattering intensity by the constant c.

Signal per particle is calculated by dividing the luminescence signal images by the number density images, and then dividing by the pixel volume. This assumes that luminescence signal varies linearly with particle seeding density. To verify linearity, Ce^{3+} and Pr^{3+} emission intensity versus seeding density/scattering signal are plotted in Figure 6. The results plotted demonstrate that the luminescence emission is proportional to seeding density/scattering signal for the entire range tested.

4. Phosphor characterization results

4.1. Absolute signal per ion

The measured luminescence intensity is used to estimate the absolute emission intensity (photons per ion) using estimated experimental and camera parameters, similar to previous work by Fond *et al.* [8]. Intensity measurements were first corrected for background signal by subtracting an average of 100 images taken at 294 K with no air flow/seeding. The number of photons emitted per ion can be written as

$$N_{ph,ion,i} = \frac{1}{\Omega/(4\pi)\eta_{opt,i}\eta_{pc,i}g_{ICCD,i}}\frac{S_i}{N_{ion}} = \frac{1}{g_i}\frac{S_i}{N_{ion}} \quad (5)$$

where $N_{ph,ion,i}$ is number of photons measured per ion for ion i, where i corresponds to Ce^{3+} (Ce) or Pr^{3+} (Pr), S_i is the measured camera signal in analog to digital units (counts) for either ion (S_{Ce} or S_{Pr}), N_{ion} is the number of ions in the collection volume, Ω is the collection solid angle, $\eta_{opt,i}$ is the optical efficiency (which accounts for transmission of optical components), $\eta_{pc,i}$ is the photocathode quantum efficiency (pe^-/photon), and $g_{ICCD,i}$ is the ICCD system gain (counts/pe^-). The total system gain, g_i (counts/photon), combines the optical and camera contributions.

From Equation 5, the signal in photons per ion depends on the average photocathode and optical efficiency, the collection solid angle, and the camera gain. The photocathode quantum efficiency and filter transmission bands, determined from manufacturer data, are plotted in Figure 4. The wavelength-averaged transmission multiplied by the photocathode quantum efficiency, weighted by the room temperature phosphor emission spectral distribution, is 0.37 pe^-/photon for Ce^{3+} and 0.18 pe^-/photon for Pr^{3+}. The total ICCD system gain was linearly interpolated from manufacturer data and is estimated to be g_{ICCD}=150 counts/pe^- for both cameras. Finally, the normalized collection solid angle, $\Omega/(4\pi)$, was estimated to be 0.0025 for Ce^{3+} and 0.0015 for Pr^{3+}. The total system gain, including optical collection efficiencies and camera efficiencies and gains, was estimated to be g_{Ce}=0.142 counts/photon for Ce^{3+} and g_{Pr}=0.037 counts/photon for Pr^{3+}. At room temperature and a fluence of 40 mJ/cm^2, $N_{ph,ion,Ce} = 2.2 \times 10^{-4}$ photons per ion, and $N_{ph,ion,Pr} = 1.0 \times 10^{-3}$ photons per ion. These values are provided in Table 2.

Table 2: Measured number of photons per particle ($N_{ph,p}$), number of photons per particle volume (V_p=0.59 μm^3), and number of photons per an ion for co-doped Ce,Pr:LuAG at 294 K for a fluence of 40 mJ/cm^2.

Phosphor	$N_{ph,p}$ [-]	$N_{ph,p}/V_p$ [μm^{-3}]	$N_{ph,ion}$ [-]
Ce,Pr:LuAG (Ce^{3+})	9.3×10^3	1.6×10^4	2.2×10^{-4}
Ce,Pr:LuAG (Pr^{3+})	4.1×10^4	7.1×10^4	1.0×10^{-3}

4.2. Luminescence temperature and fluence dependence

The per particle signal intensities as a function of laser fluence at different temperatures for Pr^{3+} are shown in Figure 7 and for Ce^{3+} in Figure 8. The best-fit lines in the plots correspond to model fits that will be described in Section 4.4. The data shown only includes data points taken within 1.25 mm of the jet centerline to avoid bias from the colder jet edge.

In Figure 7, the Pr^{3+} emission clearly varies nonlinearly with varying laser fluence with the data appearing to become more linear with increasing temperature. Pr^{3+} emission intensity, at fixed fluence, increases from 294 K to 400 K before decreasing at higher temperatures. Similar to Pr^{3+}, Figure 8 shows the nonlinear dependence on fluence for Ce^{3+} emission. In contrast with Pr^{3+}, the Ce^{3+} fluence nonlinearity appears relatively constant with temperature. The Ce^{3+} signal, at a given fluence,

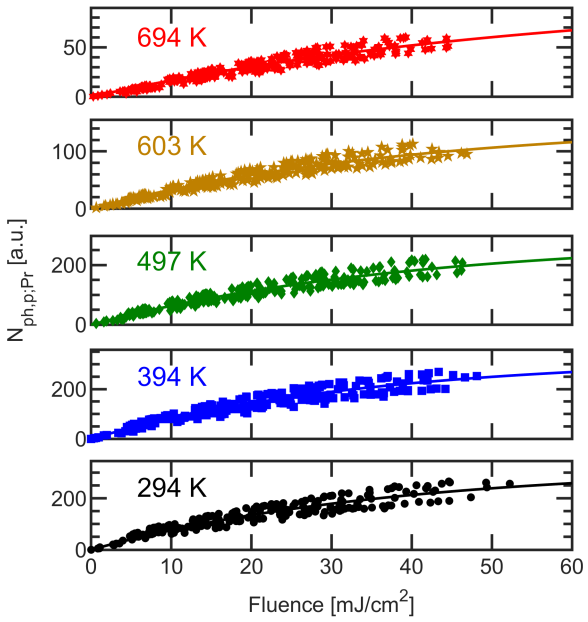

Figure 7: Praseodymium emission per particle in arbitrary units from codoped 1% (0.5%-ea.) Ce,Pr:LuAG phosphor. The Pr^{3+} collection band extends from 290 to 450 nm. All measurements are taken at an excitation wavelength of 266 nm, at temperatures from 294 to 694 K, and mean laser fluence from 5 to 35 mJ/cm^2. Solid lines represent fits to the model described in Section 4.4. Note that the vertical scale is different in each plot.

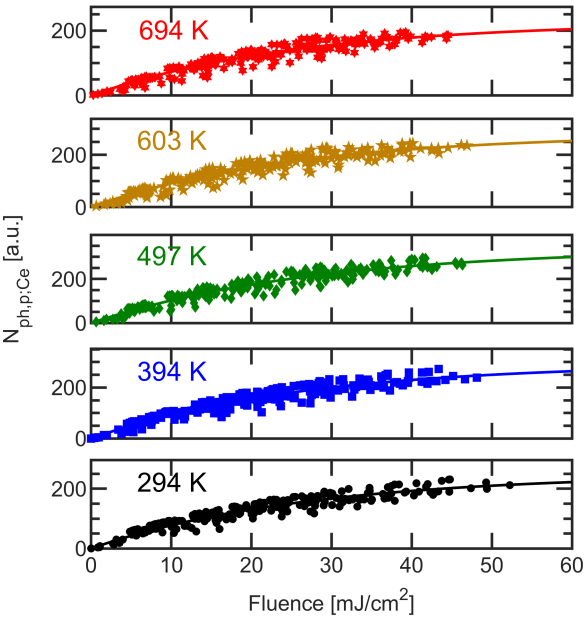

Figure 8: Cerium emission per particle in arbitrary units from codoped 1% (0.5%-ea.) Ce,Pr:LuAG phosphor. The Ce^{3+} collection band extends from 470 to 750 nm. All measurements are taken at an excitation wavelength of 266 nm at temperatures from 294 to 694 K, and mean laser fluence from 5 to 35 mJ/cm^2. Solid lines represent fits to the model described in Section 4.4. Note that the vertical scale is different in each plot.

increases with increasing temperature up to 500 K before also decreasing at higher temperatures.[1]

Several interesting trends are observed from the emission intensity data. Both Ce^{3+} and Pr^{3+} have a low average number of photons emitted per ion (≤0.001 photons/ion for all laser fluences tested), and their fluorescence signals become nonlinear at low laser fluences (below 10 mJ/cm^2). Furthermore, their fluorescence signal increases with temperature initially before quenching occurs. Trends similar to these have been seen for other phosphor materials excited using pulsed laser excitation. In particular, highly non-linear signal dependence on laser fluence has been observed for Ce:LuAG [7] and for Eu:BAM by multiple investigators [8, 21].

Applying a two-level model (neglecting thermal quenching, which is appropriate for room temperature data) using estimated ground state absorption cross-sections of ~ 10^{-19} cm^2 (based on data for singly-doped Ce:LuAG [25] and Pr:LuAG [26]), the phosphor response should be linear for fluences of >100 mJ/cm^2. This is in contrast to the nonlinearity observed at fluences <10 mJ/cm^2 for many phosphors, including the current data. Nonlinear dependence on fluence for a two-level model would also result in a large excited population, on the order of 10% or larger, which is inconsistent with the absolute signal measurements presented here. Therefore, the current observations cannot be explained through a simple two-level model and additional processes need to be considered to capture the population dynamics.

4.3. 3-level population model

The features observed in Figures 7 and 8 illustrate complex behavior that indicates the importance of processes not captured in a two-level model. To gain insight into the observed behavior, and to provide a flexible method for calibrating the temperature imaging measurements, a simplified three-level model was applied that provides the additional flexibility needed to account for nonlinearity at low fluence. Excited-state absorption is one mechanism that has been reported for both Ce^{3+} and Pr^{3+} in various host materials [27, 28] and, as will be shown, it provides a consistent explanation for the observed nonlinearity for the relatively low ion concentrations (0.5%) used in the current work.

An electronic energy-level diagram for a simplified three-level system including excited-state absorption for a single dopant ion is shown in Figure 9. In this work we make the assumption that the ions Ce^{3+} and Pr^{3+} act independently such that the three-level model can be applied independently to both ions. Referring back to Figure 1, the lowest energy level in the model, $|1\rangle$, represents the lowest $4f$ states for the ions. In the case of Pr^{3+} this level corresponds to the $^3H_4$ state, whereas for Ce^{3+} this corresponds to the $^2F_{5/2}$ state. In both cases, rapid equilibration is assumed within the level via phonon-assisted energy transfer. The intermediate level ($|2\rangle$) corresponds to the lowest energy $4f5d$ vibrational states. Rapid relaxation is assumed from higher lying $4f5d$ states due to phonon-assisted

[1] see Figure 11 to better observe the temperature dependence

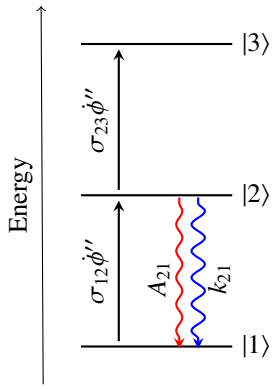

Figure 9: Sample energy-level diagram for a three-level system. Solid arrows indicate stimulated transitions, while wavy arrows indicate spontaneous transitions, and the horizontal lines indicate individual energy levels.

energy transfer. The highest energy level ($|3\rangle$) is used to represent the conduction band.

It should be noted that the three-level model is not strictly correct for Ce^{3+}. Excitation at 266 nm excites Ce^{3+} into the conduction band (see Figure 1), which then appears to deactivate quickly to the Ce^{3+} 5d level. Assuming the deactivation from the conduction band is fast compared to the lifetime of the 5d level, the three-level model should still be able to fit the observed behavior. However, the absorption cross-sections obtained are not physical and contain contributions from the relaxation process.

Energy transfer processes considered in the model, both radiative and nonradiative, are also shown in Figure 9. The model includes stimulated absorption from the ground $4f$ state ($|1\rangle$) to the excited $4f5d$ ($|2\rangle$) vibronic states of the electronic manifold and excited-state absorption from these states to the conduction band. Spontaneous radiative and nonradiative deactivation of the $4f5d$ state is included, with the nonradiative process being due to energy-assisted ionization to the conduction band (for Ce^{3+}) or intersystem cross-over (for Pr^{3+}). Excited-state absorption from $4f5d$ ($|2\rangle$) states to the conduction band ($|3\rangle$) is also included. No downward stimulated processes from either the $4f5d$ states ($|2\rangle$) or conduction band ($|3\rangle$) are included. This is justified since downward stimulated processes would occur from energies well above the bottom of the $4f5d$ potential and the bottom of the conduction band, where the thermal population is negligible following the assumed rapid equilibration of these states. Deactivation of higher states in the the conduction band following excitation (*i.e.*, those populated via ESA) are assumed to be much slower than the time span of the luminescence emission, and is neglected in the model.

Many other processes may contribute to the observed behavior such as concentration quenching, inter-ion energy transfer, cross-relaxation upconversion, carrier recombination from the conduction band, and transfer to and from trap states near the bottom of the conduction band [18]; however, the main objective here is to derive a simple model structure with sufficient flexibility to fit the observed behavior. The model selected is the simplest identified by the authors that is sufficiently complex to fit the measured fluence curves. While some of the

Table 3: Measured and best-fit (in parentheses) deactivation rate constant measured for singly-doped Ce:LuAG and Pr:LuAG from 300 to 700 K.

T [K]	$w_{21,Ce}$ [10^6 s^{-1}]	$w_{21,Pr}$ [10^6 s^{-1}]
300	16.5 (15.8)	45.0 (45.1)
400	15.8 (15.8)	47.2 (47.4)
500	15.9 (15.9)	64.3 (65.4)
600	16.3 (16.3)	- (134.3)
700	17.9 (17.7)	- (296.6)

neglected processes will become significant at higher doping percentages, at the concentrations used here they are assumed negligible [18]. Further, any additional complexity, *e.g.*, the addition of trap states or first order processes including inter-ion energy transfer, would require knowledge of additional model parameters. The three-level model is believed to be sufficient to describe the observed behaviors even for cases where inter-ion energy transfer or other mechanisms may be significant, provided the additional mechanisms are fast compared to the lifetime of the $5d$ states.

The equations describing the population evolution in the states for the simplified 3 level-model are given by

$$\frac{\mathrm{d}N_2}{\mathrm{d}t} = \sigma_{12}\dot{\phi}''N_1 - w_{21}N_2 - \sigma_{23}\dot{\phi}''N_2, \tag{6}$$

$$\frac{\mathrm{d}N_3}{\mathrm{d}t} = \sigma_{23}\dot{\phi}''N_2, \tag{7}$$

and

$$N_{tot} = N_1 + N_2 + N_3. \tag{8}$$

where the N_i (i=1,2 or 3) are the populations of the energy levels and N_{tot} is the total number of ions, σ_{12} is the ground state absorption cross-section (GSA), σ_{23} is the excited-state absorption cross-section (ESA), $\dot{\phi}''$ is the photon flux, and $w_{21} = A_{21}+k_{21}$ is the total spontaneous transition rate from $|2\rangle$ to $|1\rangle$. This spontaneous transition rate includes contributions both from radiative (A_{21}) and non-radiative (k_{21}) mechanisms. An analytic solution to these equations exists (see the appendix for the derivation and result) and is used to fit the data.

The radiative and non-radiative decay rates from $|2\rangle$ to $|1\rangle$ used in the model are taken from the curve fits to the lifetime data presented earlier in Figure 2, and several values are listed in Table 3. The laser is modeled as a 6 ns square pulse with constant photon flux (i.e., intensity). This assumption may have an impact on the fit results. However, this is expected to be small when stimulated processes dominate since the fraction of radiation emitted during the excitation process is negligible in this case. This effect may be more significant at high temperature when nonradiative deactivation rates increase.

A simple analytical expression that is useful for understanding the impact of ESA can be obtained for the population in level $|2\rangle$ if one makes the following assumptions: almost all population remains in $|1\rangle$ such that $N_1 \approx N_{tot}$, and spontaneous processes can be neglected during laser pumping. With these assumptions, by integrating Equation 6 the population at the end of laser excitation in $|2\rangle$ (N_2) is given by

$$N_2 = \frac{\sigma_{12}}{\sigma_{23}}N_{tot}[1 - \exp(-\sigma_{23}\phi'')] \tag{9}$$

where ϕ'' is the laser fluence in photons/cm^2. For small values of the product $\sigma_{23}\phi''$, the fluence dependence is linear, *i.e.*, $N_2 = \sigma_{12}N_{tot}\phi''$. For larger values of $\sigma_{23}\phi''$, the dependence on laser fluence is nonlinear and the solution approaches $N_2^\star = (\sigma_{12}/\sigma_{23})N_{tot}$ such that the maximum population in $|2\rangle$ is determined by the ratio of the GSA and ESA cross-sections. If $\sigma_{12} \ll \sigma_{23}$, only a small fraction of the total population can be retained in level $|2\rangle$. These two characteristics, non-linear fluence dependence and only a small fraction of the ions being promoted to the $4f5d$ state to potentially emit luminescence, are consistent with the observations from the luminescence signal versus fluence data shown in Figures 7 and 8, suggesting excited state absorption as a potential cause for the observed behavior.

4.4. Absorption cross-section fits

The GSA and ESA cross-sections at each temperature were determined by fitting the 3-level model (the solution of Equations 6, 7, and 8) to the emission intensity per particle measurements (presented in Figures 7 and 8). The GSA cross-section, σ_{12}, and ESA cross-section, σ_{23}, were treated as separate fit parameters for Pr^{3+} and Ce^{3+} emission (*i.e.*, Pr^{3+} and Ce^{3+} were fit independently). The model fit to the signal per particle data was included as the curves in Figures 7 and 8. Referring back to Figures 7 and 8, the model fits the shape of the data well over the entire fluence range. The scatter in the data about the fit at a given temperature is a result of both camera and fluence measurement uncertainty.

The absorption cross-sections extracted from the population model fits are plotted vs. temperature in Figure 10. At 294 K, since the absolute intensity measurements have significant uncertainty, a known value is selected for the ground state absorption (GSA) cross-section of both ions (estimated to be 1.5×10^{-19} cm^2 for Pr^{3+} using data from [16][2] supplemented with the manufacturer-provided absorption band shape, and 9×10^{-21} cm^2 for Ce^{3+} from [25][3]). For both ions there is a relatively large uncertainty in this estimate, on the order of 50%. At higher temperatures, the GSA cross-sections are measured relative to the value at 294 K, and thus are subject to the same 50% error in absolute value. For the purposes of diagnostic calibration, the best-fit ESA and GSA cross-sections were fit separately as a function of temperature; these fits are superimposed in Figure 10 in red.

As can be seen in Figure 10, the measured ESA cross-sections are much larger than the GSA cross-sections. This is

[2]Value estimated from $\sigma_{12}(\nu) = \frac{g_1}{g_0}\frac{\lambda^2}{8\pi n^2}\beta_{3H_4}Ag(\nu)$ where g_i is the degeneracy of state i, β_i is the branching ratio of state i, A is the Einstein A-coefficient, $g(\nu)$ is the absorption band shape, λ is the radiation wavelength, and n is the phosphor index of refraction.

[3]Estimated from reported absorption and doping concentration using $\ln(I/I_0) = -n\sigma l$, where I is the light intensity, n is the absorber number density, σ is the absorption cross-section, and l is the path length.

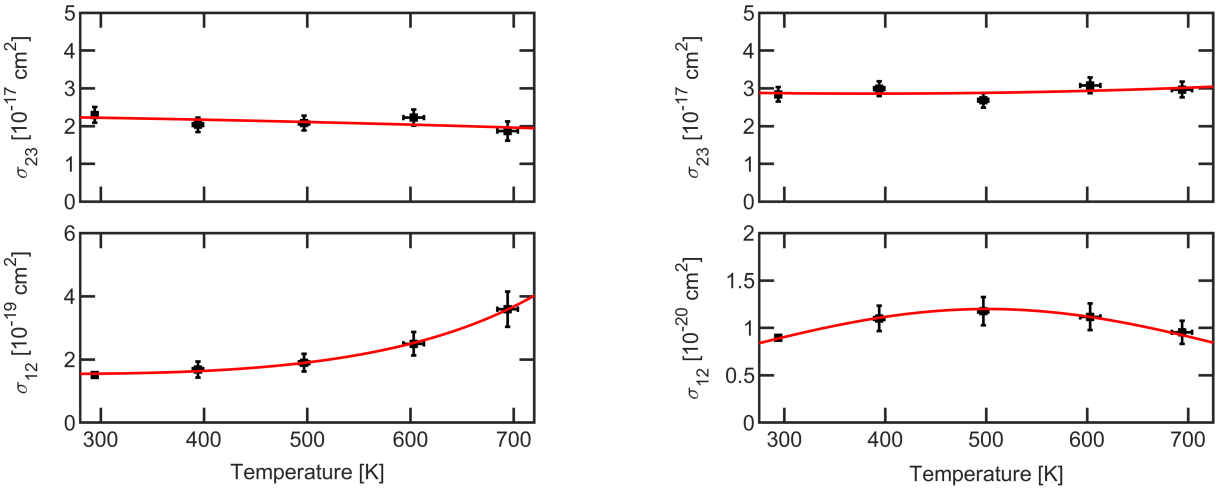

(a) Pr^{3+} GSA and ESA cross-sections

(b) Ce^{3+} GSA and ESA cross-sections

Figure 10: Absorption cross-sections (determined via curve fit to the population model) for Pr^{3+} (left; black points) and Ce^{3+} (right; black points), with best-fit curves superimposed (red curves). Vertical error bars represent 95% confidence interval in the fit parameter, and horizontal error bars represent estimated thermocouple accuracy.

expected based on the nonlinearity observed in the data and the low number of photons emitted per ion. As seen in Equation 9, the ESA cross-sections determine the curvature of the model results as a function of laser fluence and, therefore, are not affected significantly by uncertainty in the GSA cross-sections. Conversely, there is likely some bias in the ESA measurements due to errors in laser fluence determination and potential camera nonlinearity (at most 5% based on manufacturer specifications), as well as, conceptual bias stemming from model assumptions and approximations.

Although fluence non-uniformity was accounted for within the laser sheet, there is additional non-uniformity that was neglected in the out-of-plane direction. Assuming a Gaussian laser profile in the out-of-plane direction, this non-uniformity is expected to result in no more than a 50% change in the best-fit absorption cross-sections compared to a perfectly uniform fluence case.

It is difficult to determine the absolute accuracy of the resulting ESA cross-sections, but previous studies of Pr:YAG excited-state absorption have found ESA cross-sections with similar magnitude [29] to those presented here. Additionally, excited-state absorption has also been observed for Ce:YAG with large cross-sections relative to the GSA process [30]. ESA cross-sections measured in Ce:YAG for 700 nm excitation in another study [31] are similar in magnitude to those measured here but decrease by a factor of ~5 at shorter (blue) excitation wavelengths. However, the observed large UV ESA cross-sections measured here are believed to be consistent with theory. Transition rates (and absorption cross-sections) are proportional to the density of states (DOS) for the upper energy level [32]. Band structure calculations for YAG [33] show a DOS peak near 1.8 eV above the Ce^{3+} 5*d* level, then a significant decrease by 3 eV above the 5*d* level; this is consistent with the ESA measurements reported in [31]. At higher energies, particularly 4-5 eV above the Ce^{3+} 5*d* level, the DOS peaks again, suggesting an increase in absorption from the 5*d* level to the conduction band, consistent with our results. It is also worth noting that the ESA cross-sections for Ce^{3+} and Pr^{3+} are very similar in magnitude, which is consistent with this explanation as their lowest 5*d* levels occupy similar locations relative to the conduction band. From Figure 10, there appears to be little variation with temperature in both Ce^{3+} and Pr^{3+} ESA cross-sections.

It is beyond the scope of the current work to fundamentally model the observed temperature-dependence of the measured cross sections, however, the fit results provide some insights into the observed phosphor photophysics. First, the Pr^{3+} nonlinearity can be explained through the large ESA cross-section and the low signal per ion can be explained by a much smaller GSA cross-section. The signal per particle is proportional to the GSA cross-section but decreases as a result of ESA and non-radiative processes. An increase in signal could be achieved most directly by increasing the GSA cross-section, *e.g.*, by exciting on the peak of the absorption band. The initial increase in signal per ion at elevated temperatures appears to result from an increase in the GSA cross-section. No attempt is made here to interpret Ce^{3+} cross-sections due to complications related to excitation into the conduction band and potential transfer from Pr^{3+} to Ce^{3+}.

4.5. Emission intensity dependence on fluence and temperature

Per particle luminescence intensity was shown for different temperatures as a function of fluence in Figures 7 and 8 with the three-level model fit superimposed. However, the temperature dependence of the emission can be more easily observed by plotting the emission intensity versus temperature as shown in Figure 11. In Figure 11, each data point represents the average of all measurements taken at the specified temperature and

mean laser fluence within 2 mJ/cm^2 of the specified value. The solid curves are the results of the three-level model fit. The majority of the uncertainty is the result of laser fluence variation.

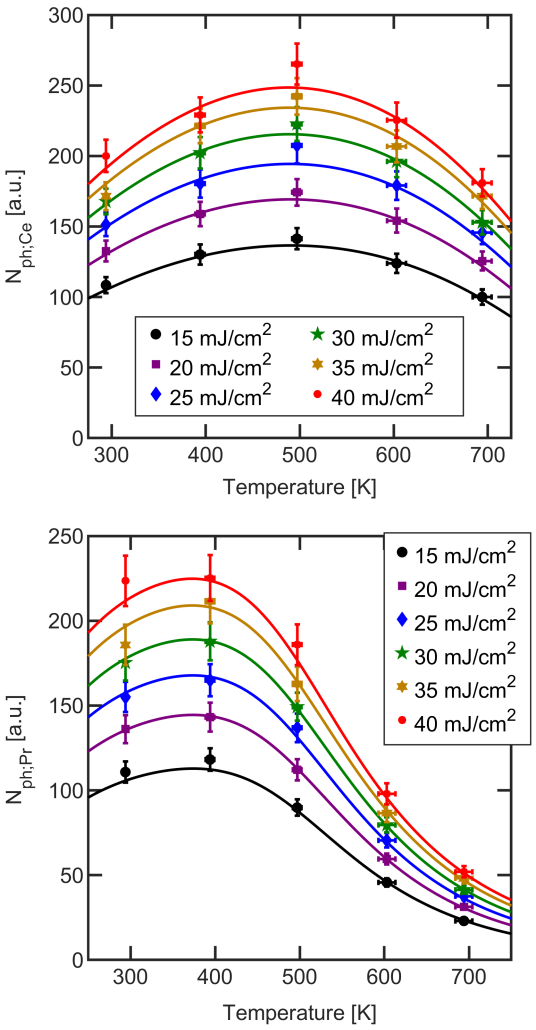

Figure 11: Measured (points) and fit (lines) relative Ce^{3+} (top) and Pr^{3+} (bottom) signal as a function of temperature and laser fluence. Errorbars include a 95% confidence interval in the fit parameters and a 5% uncertainty in laser energy. The "fit" lines are the results of the population model (Equations 6, 7 and 8), with temperature-dependent absorption cross-sections determined by the fits shown in Figure 10.

Number of photons per ion as a function of fluence and temperature, determined from the luminescence signal data (discussed in Section 4.1), are plotted in Figure 12 with signal per ion determined from the model fits superimposed. Consistent with the signal per particle discussion, number of photons emitted per ion initially increases with increasing temperature, before decreasing at higher temperatures as thermal quenching sets in. The nonlinear dependence on laser fluence is more difficult to see, but is also observed here.

Number of photons emitted per ion based on the model results are shown as the solid curves in Figure 12. While ESA does help to explain in part the relatively low signal per ion, there is about a factor of 4 difference between the measurement and model prediction for Pr^{3+}. For Ce^{3+} the predictions based

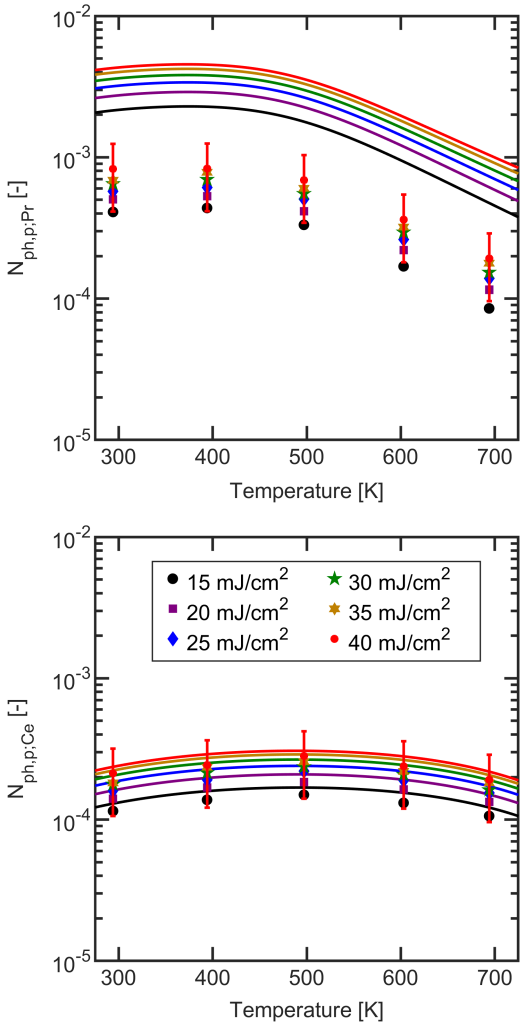

Figure 12: Measured (points) and calculated (lines) signal per ion in photons ($N_{ph,p;Ce}$ for Ce^{3+} and $N_{ph,p;Pr}$ for Pr^{3+}) for Pr^{3+} (top) and Ce^{3+} (bottom) ions. Calculated photons per ion is based on fits to three-level population model. While the Ce^{3+} results match the measurements quite well, the Pr^{3+} estimates are significantly larger than what was observed. This is likely a result of temperature- and fluence-independent loss mechanisms not considered here, and error in the absolute intensity measurement.

on the model fit are surprisingly close (within 10%) given the uncertainty in actual excitation mechanism. Uncertainty in the assumed GSA cross-sections or absolute signal measurements could account for a large portion of the difference between the model and data for Pr^{3+}, but other effects not included in the model such as energy-transfer upconversion and concentration quenching [34] may also help explain the observed difference. Since Ce^{3+} is potentially subject to the same concentration related effects as Pr^{3+}, it is possible that energy transfer from Pr^{3+} to Ce^{3+} may also be important.

The most important aspect of this data is the absolute value of number of photons emitted per ion, which is always less than 0.001. This indicates that fewer than 0.1% of ions are emitting photons, and in the case of Ce^{3+} less than 0.03% of ions are emitting photons. At room temperature, thermal quenching is not a significant loss mechanism, indicating that less than 0.1%

of ions are excited to a $4f5d$ state. These results are consistent with the explanation of ESA as a low-fluence loss mechanism.

ESA may be a significant loss mechanism in other phosphors as well; in particular, Eu:BAM exhibits strongly non-linear excitation that is not consistent with a simple two-level model [8]. However, there are additional mechanisms that may be significant in Eu:BAM (*e.g.*, energy transfer upconversion), especially at the high (10%) doping concentrations typically used.

4.6. Diagnostic calibration, sensitivity, and bias

The calibration function used for temperature measurements is derived from the three-level population model presented in Section 4.3, and the absorption cross-section fits in Figure 10. The emission signal intensity of a phosphor neglecting spontaneous processes during laser excitation can be described as

$$S_i = N_i^\star(T;\phi'')\, A_i\, \tau_i(T)\, g_i, \tag{10}$$

where $N_i^\star(T;\phi'')$ is the excited population following the laser pulse for phosphor i, A_i is the Einstein A-coefficient, $\tau_i(T)$ is the luminescence lifetime, and g_i is the overall collection system gain for phosphor i,. The luminescence intensity ratio R can then be expressed as

$$\begin{aligned} R &= \frac{S_{Ce}(T;\phi'')}{S_{Pr}(T;\phi'')}\,\frac{S_{Pr}(T_0;\phi_0'')}{S_{Ce}(T_0;\phi_0'')} \\ &= \frac{N_{Ce}^\star(T;\phi'')}{N_{Pr}^\star(T;\phi'')}\,\frac{N_{Pr}^\star(T_0;\phi_0'')}{N_{Ce}^\star(T_0;\phi_0'')}\,\frac{\tau_{Ce}(T)}{\tau_{Pr}(T)}\,\frac{\tau_{Pr}(T_0)}{\tau_{Ce}(T_0)} \end{aligned} \tag{11}$$

where the subscript 0 is used to indicate the reference condition. For the data presented here, the reference temperature is 294 K, and the reference fluence is dependent on the image location, and is approximately unchanged throughout the experiment (*i.e.*, $\phi_0'' \approx \phi''$). All parameters required to evaluate Equation 11 were determined and presented in Section 4.4 and Figure 2.

In Figure 13, the measured ratio is compared to the model fit over a range of measured temperatures and laser fluences. The laser fluence here is not exactly equal to that at which the flat-field correction is taken, and as a result there is some additional scatter in the calibration data points. The model fit represents the ratios well, with about a 2% residual on average and a maximum residual of about 5% at 394 K. From this plot, ratios at high temperature (near 700 K) show fluence dependence which could lead to a significant fluence bias; however, below 600 K laser fluence appears to have little effect on the ratio.

The fractional sensitivity of the ratio to any quantity x is defined as

$$\xi_x = \frac{1}{R}\frac{\partial R}{\partial x}, \tag{12}$$

and can be calculated directly from the calibration function. Figure 14 plots both the fractional temperature sensitivity (top) and the fractional fluence sensitivity (bottom). For both plots, the reference fluence is held constant at the specified value and the reference temperature is 294 K.

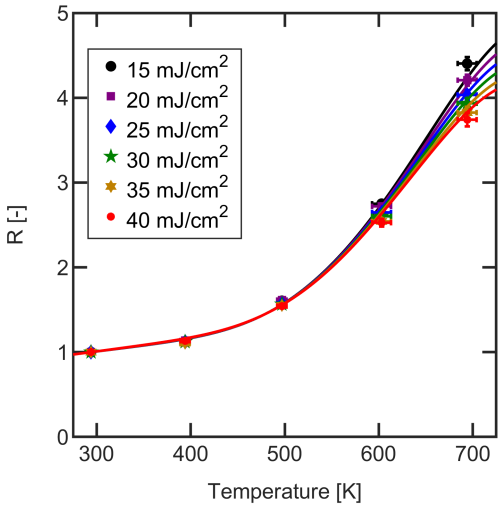

Figure 13: Expected co-doped ratio (lines) and measured ratio (points) as a function of fluence and temperature.

Figure 14 shows a temperature sensitivity of greater than 0.25%/K from about 450-700 K, with a peak of about 0.5%/K near 600 K that decreases with increasing fluence. The temperature sensitivity appears to be minimized in the 300 to 400 K range. The temperature sensitivity of the ratio is directly a result of the difference in the ions' thermal quenching behavior. Since Pr^{3+} has a 50% quenching temperature in LuAG of approximately 550 K and Ce^{3+} has a 50% quenching temperature closer to 850 K [16], the observed temperature sensitivity can be attributed almost entirely to Pr^{3+} quenching. From [16], temperature sensitivity typically peaks near the 50% quenching temperature which is also consistent with these findings. The measured sensitivity of greater than 0.25%/K up to 700 K illustrates the potential of this phosphor to extend the temperature measurement range for co-doped APT.

The fractional fluence sensitivity is close to zero in the temperature range from 300 to 500 K. Above ~500 K, the magnitude of the fluence sensitivity increases significantly with increasing temperature. Further, as fluence increases, the ratio fluence sensitivity magnitude decreases. This can be explained by the nonlinearity of the excitation process. As fluence is increased towards the saturation limit, the emission intensity for each ion approaches a constant limiting value, and likewise the intensity ratio approaches a constant limiting value.

The fractional fluence sensitivity and temperature sensitivity together can be used to estimate the temperature measurement uncertainty resulting from ratio sensitivity to the laser fluence. The temperature measurement uncertainty due to a small fluence uncertainty is given by the ratio of the fluence sensitivity to the temperature sensitivity, or

$$b_{T;E''} \approx \frac{\xi_{E''}}{\xi_T} b_{E''}, \tag{13}$$

where b_i is the uncertainty in the quantity i. This quantity, per unit uncertainty in laser fluence, is plotted in Figure 15 (left). As an example, at 700 K and a fluence of 50 mJ/cm^2, a 10% flu-

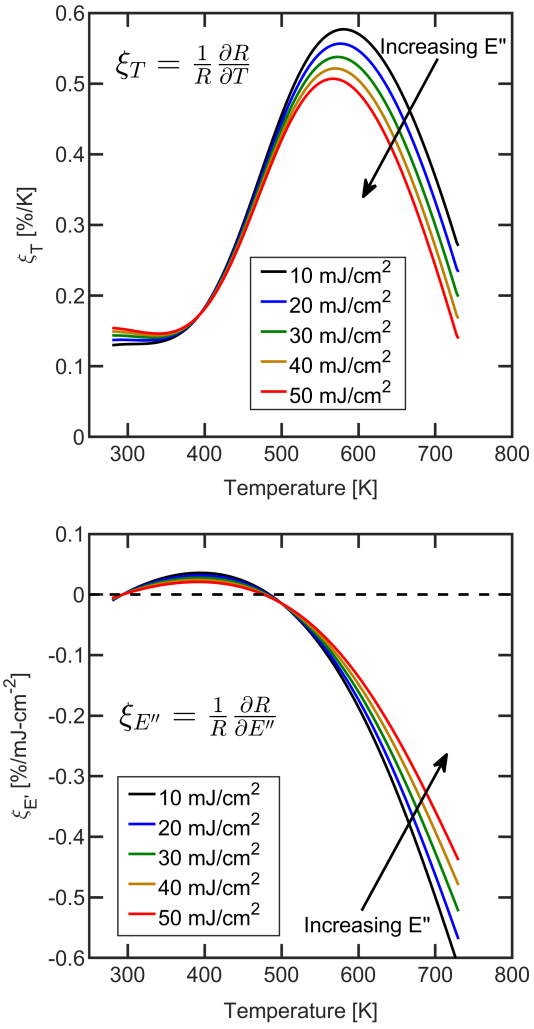

Figure 14: Sensitivity of measured luminescence intensity ratio to both temperature (top) and fluence (bottom) from 300 to 700 K for several values of laser fluence. The reference condition is chosen to be at 294 K, and constant fluence.

ence variation (±5 mJ/cm^2) results in a temperature uncertainty of less than 1%.

The error associated with uncertainty in the reference condition can be estimated in a similar manner. The reference condition is defined by two values, namely the reference laser fluence and the reference temperature. As before, the target reference temperature is taken to be 294 K, and the laser fluence is assumed to be unchanged throughout the experiment. The temperature measurement uncertainty resulting from uncertainty in the reference values can be written as

$$b_{T;T_0} = \frac{\xi_{T_0}}{\xi_T} b_{T_0} \tag{14}$$

for reference temperature, and as

$$b_{T;E''_0} = \frac{\xi_{E''_0}}{\xi_T} b_{E''_0} \tag{15}$$

for the reference fluence.

The calculated temperature uncertainties are plotted in the right two panels of Figure 15. Temperature measurement uncertainty resulting from uncertainties in either the reference fluence or reference temperature have their largest magnitudes at low temperatures (near 300 K) and at high temperature (near 700 K); this is a result of the low ratio temperature sensitivity in these regions. Temperature measurement uncertainty due to uncertainty in the reference fluence is strongly fluence dependent at low temperature. The goal of the flatfield correction is to normalize the calibration function to unity at the reference temperature; thus an error in reference fluence biases the calibration curve and scales it by a constant factor. Since the temperature sensitivity is low near 300 K, a small uncertainty in the fluence can result in a relatively large temperature error. As the mean fluence increases, the phosphor approaches a saturation condition where small changes in fluence have little effect on the excited population, reducing the uncertainty magnitude. It should be noted that within the range of 450-700 K a 5% error in the reference temperature or fluence results in at most a few percent error in the measured temperature.

To avoid or reduce uncertainties in future experiments using this phosphor, it is advantageous to operate at high laser fluence near 50 mJ/cm^2 as the measurement uncertainty (per unit fluence uncertainty) is reduced. Conversely, the measurement uncertainty resulting from error in the reference temperature increases with fluence due to a reduced temperature sensitivity. This effect should be negligible if the reference condition is at the ambient temperature and can be measured to a high degree of accuracy. However, if the reference temperature is elevated, it is beneficial to choose the reference somewhere between 450 and 650 K where temperature sensitivity is maximized, minimizing the effect.

So far, only small changes in fluence have been considered. However, it is likely that in complicated experimental geometries, fluence could be varied significantly (on the order of, say, 50%) due to turbulent density gradients or beam-steering effects, or other uncontrolled factors. Since the fluence variation is large, the sensitivity analysis used previously may not be valid. Instead, a separate calculation was performed where the temperature error is calculated for a 50% bias in fluence (both positive and negative) using the two-dimensional calibration function. The results are plotted for several fluence values in Figure 16 from 300 to 700 K. Below 600 K, the fluence bias is very small, on the order of 5 K or less. However, above 600 K, the error grows significantly as the diagnostic becomes sensitive to fluence. Note that since the fluence bias is large, the temperature error depends on the sign of the fluence error. For the cases shown here, the temperature error is larger for a positive fluence bias.

5. Heated jet temperature imaging

Temperature imaging was performed using a subset of the validation data. The experimental setup was discussed in Section 3, but in this case only data taken with a laser energy of 6 mJ (corresponding to 33 mJ/cm^2 mean fluence) is included. As with the characterization experiments, a flatfield correction is

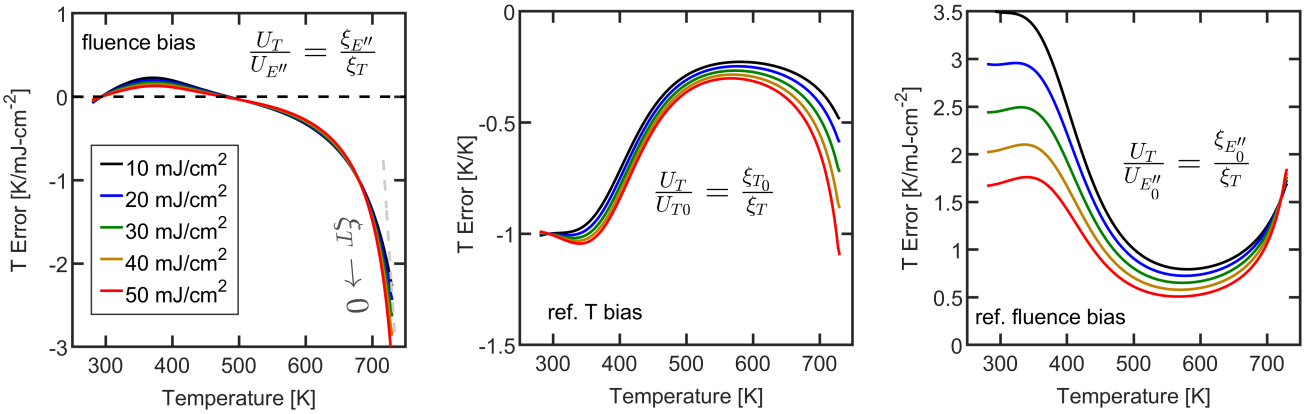

Figure 15: Estimated temperature measurement uncertainty resulting from uncertainty in the laser fluence (left), reference temperature (middle), and reference laser fluence (right) for a range of experimental conditions. The reference temperature is 294 K in all cases.

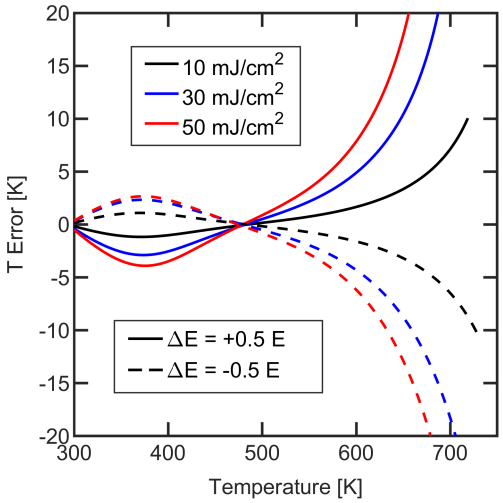

Figure 16: Calculated temperature error due to a 50% fluence bias for several "target" fluence cases, from 300 to 700 K.

applied to the data using the average room temperature (294 K) images. Laser fluence is estimated for both the flatfield image and the experimental images separately based on Mie scattering, and laser fluence variation is accounted for using the calibration function. A fast Fourier Transform-based phase correlation (see [35] for a thorough discussion of this and other registration methods) is used for image registration to identify the relative translation between the Ce^{3+} and Pr^{3+} images, and the Ce^{3+} images are shifted and resampled using a bicubic interpolation scheme. Only translation was considered in the image registration, no rotation or distortion correction were needed or applied. The signal images were software binned 2×2, resulting in a final object plane pixel length of 0.52 mm. No additional filtering is applied to the images. The final spatial resolution of the imaging system is estimated to be between 1 and 1.12 lp/mm based on an image of the 1951 USAF resolution test chart that was taken with the Ce^{3+} camera and binned to the final measurement size; signal modulation at 1-1.12 lp/mm is approximately 50%.

5.1. *Temperature imaging results*

A series of single-shot temperature and ratio images are shown for each jet exit temperature in the first and third rows (from top) of Figure 17. Variation in both the ratio and temperature are evident near the edges of the jet for the 497, 603, and 694 K images. The 294 K and 694 K images both exhibit some empty data points on the interior of the jet. Since these temperatures are very near the local extrema of the calibration function, ratio fluctuations due to noise (or due to fluence uncertainty) result in measurements outside the range of the calibration function and are not evaluated. In both cases, this results in error in the mean temperature. For the 694 K case the measurement is biased towards colder values, and for the 294 K the measurement is biased towards hotter values.

The median temperature and ratio images are likewise shown in Figure 17 (second and fourth from top). Similar to the single-shot images, some temperature and ratio variation is evident across the width of the jet. Additionally in the 694 K median ratio image, some ratio variation is evident in the vertical direction resulting from fluence non-uniformity; however, as the measured temperature is a function of both fluence and ratio, this variation is expected.

5.2. *Ratio precision*

For each single-shot image, the fractional ratio precision and seeding density are calculated and plotted in the top of Figure 18. Precision statistics are taken in a 2.5 mm wide, 5 mm tall box centered in the middle of the image; this corresponds to the region of peak laser intensity, and temperature is uniform in this region. Although the seeding density is constant on average, there is shot-to-shot (temporal) variation in seeding that allows us to sample a range of densities. The measured ratio uncertainty at all temperatures varies from about 20% at the lowest seeding densities (around 100 particles per mm^3) down to about 7% at the highest seeding densities (around 300 particles per mm^3). The ratio precision is approximately proportional to

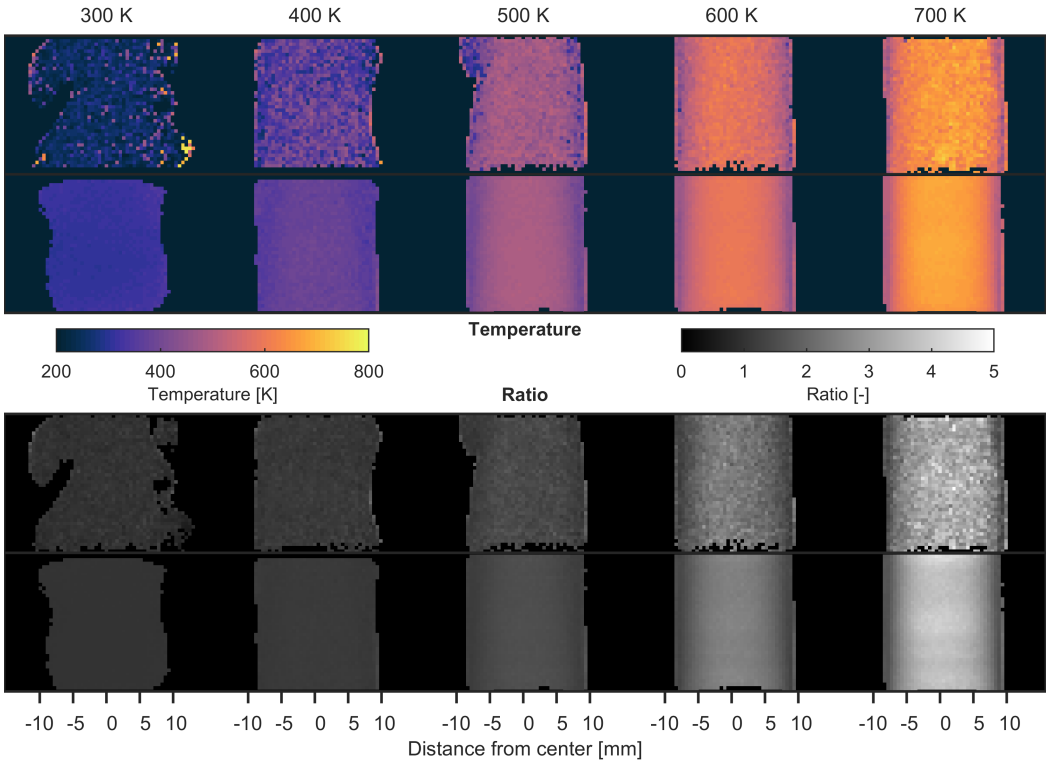

Figure 17: Temperature and corresponding ratio images, both single-shot and median, for each measured temperature. From top: single-shot temperature, median temperature, single-shot ratio, median ratio. Estimated jet temperature from left to right is 294 K, 394 K, 497 K, 603 K, and 694 K.

the inverse square-root of the seeding density as expected for a linear signal-dependence on particle number density in the shot-noise limit. The ratio uncertainties are not significantly temperature dependent, with very similar values up to the 603 K case where the ratio is expected to vary significantly throughout the image due to fluence non-uniformity. Ratio uncertainties do increase slightly at 694 K, and this is expected due to decreased signal from thermal quenching.

Distributions of the ratio fluctuations are additionally shown in the bottom of Figure 18. In this case, to avoid bias due to variation in the laser pulse energy and jet temperature fluctuations, each ratio image is mean-subtracted before calculating the ratio probability density functions (PDFs). The mean-subtracted PDF is then shifted to the mean value of the entire data set. Up to the 603 K case, the ratio distributions appear to be Gaussian.

5.3. Temperature precision

Single-shot temperature precision (per image) is plotted against the image-mean seeding density in the top of Figure 19. Similar to the ratio (see Figure 18), the temperature precision improves with increasing number density, and appears to follow the inverse-square-root behavior expected for a shot-noise-limited diagnostic. Although the ratio precision is largely independent of temperature for this data set, the temperature precision varies significantly with temperature due to the change in ratio fractional sensitivity with increasing temperature. Specifically for the 294 K case, single-shot temperature precision worse than 20% is observed at low seeding densities; this is the result of very low temperature sensitivity at 300 K. The 497, 603, and 694 K cases all have better than 5% temperature precision at seeding densities above approximately 150 particles per mm^3.

The bottom of Figure 19 shows the temperature probability density functions for each data set. The images are again mean-subtracted to remove shot-to-shot variation in the mean before calculating the distribution, and are shifted to the overall mean temperature. The measured temperature precision ("s") and error in the mean ("b") are displayed on the plot for each temperature. The bias value is determined as the difference between the thermocouple measurement and the mean of the distribution.

At 294 and 394 K, the diagnostic has poor precision due to low temperature sensitivity, but the temperature uncertainties are consistent with the measured ratio precision according to Equation 2. Above 400 K, the temperature sensitivity improves significantly with single-shot temperature precision of 22 and 23 K at 497 and 603 K, respectively. At 694 K, particle number density is reduced and much of the Pr^{3+} signal has been quenched resulting in a temperature precision of 32 K.

Although the sensitivity is still relatively high, there is some non-negligible uncertainty in the fluence measurement which is potentially affecting the temperature measurement. This fluence uncertainty, in addition to calibration bias and the reduced range of the calibration function, is at least partially responsible for the non-zero error in the mean temperature. These effects are expected and observed to be dominant at the lowest (294

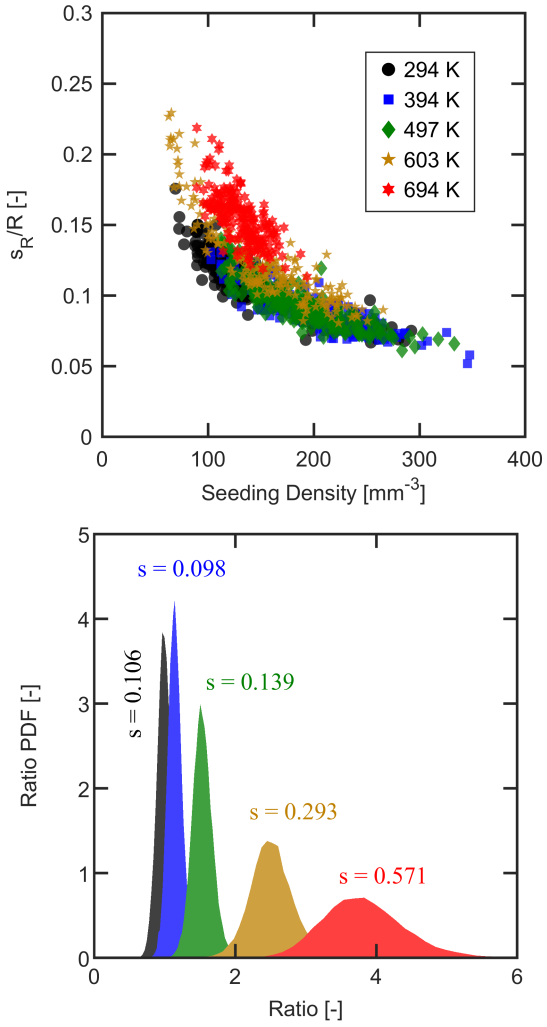

Figure 18: Ratio precision vs. seeding density (top) and probability density functions for the ratio measurements at the five mean jet temperatures (bottom). The symbol "s" indicates the single-shot ratio precision.

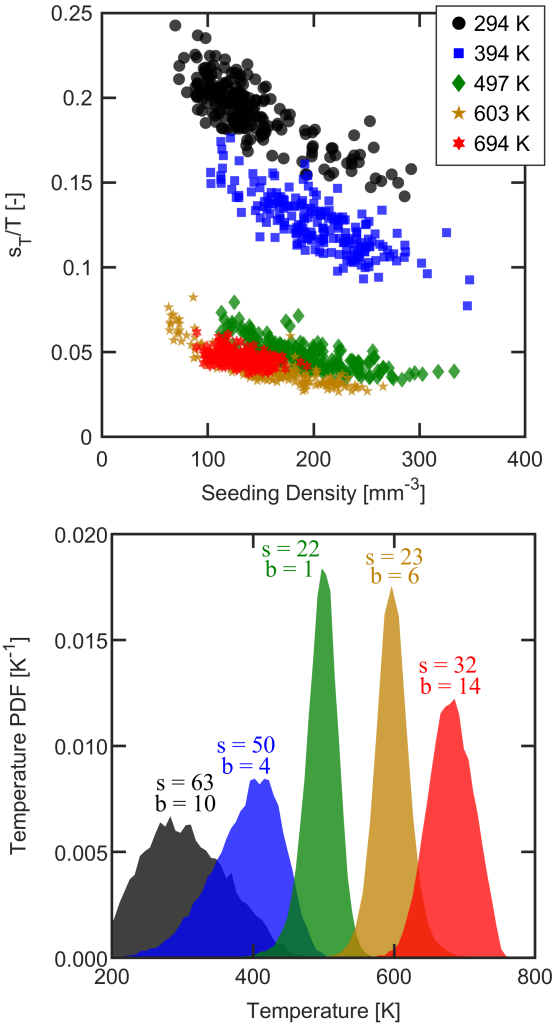

Figure 19: Scatter plot vs. seeding density (top) and distribution (bottom) of temperature measurements for five mean jet temperatures. The symbol "b" indicates the error in the mean and "s" indicates the single-shot temperature precision.

& 394 K) and highest temperatures (694 K). Note that at 694 K, unlike in the ratio distribution, the temperature distribution appears to be symmetric and Gaussian. Since the fluence non-uniformity is accounted for in the calibration procedure, the fluence bias is greatly reduced.

6. Conclusions

Aerosol phosphor thermometry using co-doped phosphors provides a possible avenue for high-precision temperature measurements at combustion relevant conditions. The primary goal of this study was to evaluate and characterize a new phosphor for co-doped APT, Ce,Pr:LuAG. An imaging approach using the Ce,Pr:LuAG co-doped phosphor seeded into a heated jet was used for phosphor characterization and to demonstrate temperature imaging using the technique at atmospheric pressure for temperatures up to 700 K.

Phosphor linearity with laser fluence was investigated as a function of temperature and a three-level population model was applied to describe the data. The population model was fit to the experimental data, providing a convenient calibration function for use when applying the diagnostic for temperature imaging. The ground state absorption cross-sections and excited-state absorption cross-sections were used as the fitting parameters and the values determined from the model fit were consistent with previous measurements and theory. The population model provides insight into the potential effect of excited-state absorption on emission intensity. The results of the three-level model fit were also used to estimate the effect of fluence bias on the data. Temperature sensitivity for the co-doped APT technique using Ce,Pr:LuAG peaks near 600 K at slightly above 0.5%/K, and a peak single-shot temperature precision of 22 K was achieved at 500 K at an average seeding density of approximately 150 mm^{-3}. This work extends the temperature range of co-doped APT from 500 K (with Ce,Pr:YAG) to approximately 700 K and demonstrates how the temperature imaging range can be tuned by changing phosphor host composition.

Acknowledgements

Research was sponsored by the Army Research Office and was accomplished under Grant Number W911NF-19-1-0238. The views and conclusions contained in this document are those of the authors and should not be interpreted as representing the official policies, either expressed or implied, of the Army Research Office or the U.S. Government. The U.S. Government is authorized to reproduce and distribute reprints for Government purposes notwithstanding any copyright notation herein.

References

[1] A. Omrane, P. Petersson, M. Alden, M. A. Linne, Simultaneous 2D flow velocity and gas temperature measurements using thermographic phosphors, Applied Physics B-Lasers and Optics 92 (1) (2008) 99–102.

[2] C. Abram, B. Fond, F. Beyrau, High-precision flow temperature imaging using ZnO thermographic phosphor tracer particles, Optics express 23 (15) (2015) 19453–19468.

[3] A. O. Ojo, B. Fond, C. Abram, B. G. Van Wachem, A. L. Heyes, F. Beyrau, Thermographic laser doppler velocimetry using the phase-shifted luminescence of BAM:Eu^{2+} phosphor particles for thermometry, Optics express 25 (10) (2017) 11833–11843.

[4] L. Fan, Y. Gao, A. Hayakawa, S. Hochgreb, Simultaneous, two-camera, 2D gas-phase temperature and velocity measurements by thermographic particle image velocimetry with zno tracers, Experiments in Fluids 58 (4) (2017) 34.

[5] N. J. Neal, J. Jordan, D. Rothamer, Simultaneous measurements of in-cylinder temperature and velocity distribution in a small-bore diesel engine using thermographic phosphors, SAE International Journal of Engines 6 (1) (2013) 300–318.

[6] D. Witkowski, D. A. Rothamer, Scattering referenced aerosol phosphor thermometry, Measurement Science and Technology 30 (4) (2019) 044003.

[7] D. Witkowski, J. Herzog, D. A. Rothamer, High-precision aerosol phosphor thermometry with Ce^{3+} and Pr^{3+} co-doped into lutetium aluminum garnet, 11th U.S. National Combustion Meeting.

[8] B. Fond, C. Abram, F. Beyrau, Characterisation of the luminescence properties of BAM:Eu^{2+} particles as a tracer for thermographic particle image velocimetry, Applied Physics B 121 (4) (2015) 495–509.

[9] H. Lee, B. Böhm, A. Sadiki, A. Dreizler, Turbulent heat flux measurement in a non-reacting round jet, using BAM:Eu^{2+} phosphor thermography and particle image velocimetry, Applied Physics B 122 (7) (2016) 209.

[10] F. Zentgraf, M. Stephan, E. Berrocal, B. Albert, B. Böhm, A. Dreizler, Application of structured illumination to gas phase thermometry using thermographic phosphor particles: a study for averaged imaging, Experiments in Fluids 58 (7) (2017) 82.

[11] M. Stephan, F. Zentgraf, E. Berrocal, B. Albert, B. Böhm, A. Dreizler, Multiple scattering reduction in instantaneous gas phase phosphor thermometry: applications with dispersed seeding, Measurement Science and Technology 30 (5) (2019) 054003.

[12] C. Abram, B. Fond, F. Beyrau, Temperature measurement techniques for gas and liquid flows using thermographic phosphor tracer particles, Progress in Energy and Combustion Science 64 (2018) 93–156.

[13] J. Brübach, C. Pflitsch, A. Dreizler, B. Atakan, On surface temperature measurements with thermographic phosphors: A review, Progress in Energy and Combustion Science 39 (1) (2013) 37–60.

[14] D. Witkowski, D. A. Rothamer, A novel strategy to improve the sensitivity of aerosol phosphor thermometry using co-doped phosphors, Proceedings of the Combustion Institute 37 (2) (2019) 1393–1400.

[15] P. Dorenbos, A review on how lanthanide impurity levels change with chemistry and structure of inorganic compounds, ECS Journal of Solid State Science and Technology 2 (2) (2013) R3001–R3011.

[16] D. Witkowski, D. A. Rothamer, Emission properties and temperature quenching mechanisms of rare-earth elements doped in garnet hosts, Journal of Luminescence 192 (2017) 1250–1263.

[17] H. Yamamoto, Luminescence of a localized center, in: W. M. Yen, S. Shionoya, H. Yamamoto (Eds.), Phosphor Handbook, 2nd Edition, CRC Press/Taylor and Francis, Boca Raton, FL, 2007, book section 2.3, pp. 35–47.

[18] A. Lenef, M. Raukas, J. Wang, C. Li, Phosphor performance under high intensity excitation by InGaN laser diodes, ECS Journal of Solid State Science and Technology 9 (1) (2020) 016019.

[19] D. Witkowski, D. A. Rothamer, A methodology for identifying thermographic phosphors suitable for high-temperature gas thermometry: application to Ce^{3+} and Pr^{3+} doped oxide hosts, Applied Physics B 123 (8) (2017) 226.

[20] J. Ogiegło, A. Zych, T. Jüstel, A. Meijerink, C. Ronda, Luminescence and energy transfer in $Lu_3Al_5O_{12}$ scintillators co-doped with Ce^{3+} and Pr^{3+}, Optical materials 35 (3) (2013) 322–331.

[21] D. Witkowski, D. A. Rothamer, Investigation of aerosol phosphor thermometry (APT) measurement biases for Eu:BAM, Applied Physics B 124 (10) (2018) 202.

[22] D. Nagasawa, N. Mondrik, J. Marshall, D. DePoy, L. Schmidt, B. Hill, L. Turner, J. Rheault, Throughput of commercial photographic camera lenses for use in astronomical systems, in: Ground-based and Airborne Instrumentation for Astronomy VI, Vol. 9908, International Society for Optics and Photonics, 2016, p. 99085C.

[23] P. Chỳlek, G. Grams, R. Pinnick, Light scattering by irregular randomly oriented particles, Science 193 (4252) (1976) 480–482.

[24] T. Justel, Phosphor Information and Spectra Access (PISA) (2019 (accessed October 2, 2019)).
URL `fh-muenster.de/ciw/personal/professoren/juestel/pisa.php`

[25] H.-L. Li, X.-J. Liu, L.-P. Huang, Fabrication of transparent cerium-doped lutetium aluminum garnet (LuAG:Ce) ceramics by a solid-state reaction method, Journal of the American Ceramic Society 88 (11) (2005) 3226–3228.

[26] T. Yanagida, A. Yoshikawa, A. Ikesue, K. Kamada, Y. Yokota, Basic properties of ceramic Pr:LuAG scintillators, IEEE Transactions on Nuclear Science 56 (5) (2009) 2955–2959.

[27] A. Lenef, J. Kelso, Y. Zheng, M. Tchoul, Radiance limits of ceramic phosphors under high excitation fluxes, in: Current Developments in Lens Design and Optical Engineering XIV, Vol. 8841, International Society for Optics and Photonics, 2013, p. 884107.

[28] M. Laroche, S. Girard, J. Margerie, R. Moncorgé, M. Bettinelli, E. Cavalli, Experimental and theoretical investigation of the $4f^n 4f^{n-1}5d$ transitions in YPO_4:Pr^{3+} and YPO_4:Pr^{3+},Ce^{3+}, Journal of Physics: Condensed Matter 13 (4) (2001) 765.

[29] Y. Cheung, S. Gayen, Excited-state absorption in Pr^{3+}:$Y_3Al_5O_{12}$, Physical Review B 49 (21) (1994) 14827.

[30] R. Jacobs, W. Krupke, M. Weber, Measurement of excited-state-absorption loss for Ce^{3+} in $Y_3Al_5O_{12}$ and implications for tunable 5d→4f rare-earth lasers, Appl. Phys. Lett.;(United States) 33 (5).

[31] D. Hamilton, S. Gayen, G. Pogatshnik, R. Ghen, W. Miniscalco, Optical-absorption and photoionization measurements from the excited states of Ce^{3+}:$Y_3Al_5O_{12}$, Physical Review B 39 (13) (1989) 8807.

[32] J. J. Sakurai, E. D. Commins, Modern quantum mechanics, revised edition, Addison-Wesley, 1994.

[33] A. B. Muñoz-García, E. Anglada, L. Seijo, First-principles study of the structure and the electronic structure of yttrium aluminum garnet $Y_3Al_5O_{12}$, International Journal of Quantum Chemistry 109 (9) (2009) 1991–1998.

[34] D. L. Dexter, J. H. Schulman, Theory of concentration quenching in inorganic phosphors, The Journal of Chemical Physics 22 (6) (1954) 1063–1070.

[35] L. G. Brown, A survey of image registration techniques, ACM computing surveys (CSUR) 24 (4) (1992) 325–376.

Appendix A. Analytic solution to population model

The population model used in this work contains only first order terms as a result of the low fluence and doping concentrations used here. In this case, the rate equations can be rewritten as

$$\frac{\mathrm{d}\vec{n}}{\mathrm{d}t} = (\mathbf{B}\dot{\phi}'' + \mathbf{W})\vec{n}, \tag{A.1}$$

where the vector $\vec{n}$ represents the population fraction in each state i, $\dot{\phi}''$ is the photon flux rate, and the (singular) matrices $\mathbf{B}$ and $\mathbf{W}$ represent stimulated and spontaneous processes, respectively. Here, these matrices are

$$\mathbf{B} = \begin{bmatrix} -\sigma_{12} & 0 & 0 \\ \sigma_{12} & -\sigma_{23} & 0 \\ 0 & \sigma_{23} & 0 \end{bmatrix} \tag{A.2}$$

and

$$\mathbf{W} = \begin{bmatrix} 0 & w_{21} & 0 \\ 0 & -w_{21} & 0 \\ 0 & 0 & 0 \end{bmatrix}. \tag{A.3}$$

Equation A.1 is a first order linear ordinary differential equation system, and has the solution

$$\vec{n} = e^{\mathbf{B}\phi'' + \mathbf{W}t}\vec{n}_0, \tag{A.4}$$

where $\vec{n}_0$ is the initial population vector (here assumed to be concentrated in the ground state, or $\vec{n}_0 = |1\rangle$), and ϕ'' is the integrated photon flux at time t. This solution and method is valid for any number of states and first order processes. The solution (Equation A.4) is a matrix exponential which can be simplified and evaluated by eigendecomposition using the identity

$$e^{\mathbf{M}} = \mathbf{P}e^{\mathbf{D}}\mathbf{P}^{-1} \tag{A.5}$$

for a matrix $\mathbf{M}$ with eigendecomposition

$$M = \mathbf{P}\mathbf{D}\mathbf{P}^{-1} \tag{A.6}$$

by eigenvector matrix $\mathbf{P}$ and diagonal eigenvalue matrix $\mathbf{D}$.

A useful approximation can be found for low fluence cases. The solution to any n-level first-order system (Equation A.4) is a sum of n exponentials. At sufficiently low fluence, only the largest exponential term will dominate and, noting that $\mathbf{W}$ and $\mathbf{B}$ are singular, the population in $|i\rangle$ is approximately

$$n_i = c(1 - e^{-\lambda}) \tag{A.7}$$

where λ is the smallest non-zero entry in $\mathbf{D}$, and c is a proportionality constant. Choosing c to enforce the linear limit, $n_i \approx \sigma_{1i}\phi''$, results in

$$n_i = \frac{\sigma_{1i}\phi''}{\lambda}(1 - e^{-\lambda}). \tag{A.8}$$

In the limit where either spontaneous or stimulated processes are negligible, the eigenvalues take on the form $\lambda \approx \sigma_{eff}\phi''$ where σ_{eff} is an effective absorption cross-section, or $\lambda \approx w_{eff}t$ where w_{eff} is an effective spontaneous rate constant, respectively.

The eigenvalues of three-level model presented here can be solved analytically by matrix decomposition, as the characteristic polynomial of $\mathbf{B}\phi'' + \mathbf{W}t$ is quadratic. The eigenvalue decomposition of $\mathbf{B}\phi'' + \mathbf{W}t$ is

$$e^{\mathbf{B}\phi'' + \mathbf{W}t} = \mathbf{P}e^{\mathbf{D}}\mathbf{P}^{-1}, \tag{A.9}$$

where

$$\mathbf{P} = \begin{bmatrix} 0 & \frac{\lambda_+}{\sigma_{23}\phi''} - 1 & \frac{\lambda_-}{\sigma_{23}\phi''} - 1 \\ 0 & -\frac{\lambda_+}{\sigma_{23}\phi''} & -\frac{\lambda_-}{\sigma_{23}\phi''} \\ 1 & 1 & 1 \end{bmatrix} \tag{A.10}$$

and

$$\mathbf{D} = \begin{bmatrix} 0 & 0 & 0 \\ 0 & -\lambda_+ & 0 \\ 0 & 0 & -\lambda_- \end{bmatrix} \tag{A.11}$$

and the eigenvalues $\lambda_\pm$ are given by

$$\begin{aligned} \lambda_\pm = &\frac{\sigma_{12}\phi'' + \sigma_{23}\phi'' + w_{21}t}{2} \\ &\pm \frac{\sqrt{(\sigma_{12}\phi'' + \sigma_{23}\phi'' + w_{21}t)^2 - 4\sigma_{12}\sigma_{23}\phi''^2}}{2}. \end{aligned} \tag{A.12}$$

Carrying out the matrix multiplication results in

$$\vec{n} = \begin{bmatrix} \frac{e^{-\lambda_+}\lambda_-(\lambda_+ - \sigma_{23}\phi'') - e^{-\lambda_-}\lambda_+(\lambda_- - \sigma_{23}\phi'')}{\sigma_{23}\phi''(\lambda_+ - \lambda_-)} \\ \frac{\lambda_+\lambda_-}{\sigma_{23}\phi''(\lambda_+ - \lambda_-)}(e^{-\lambda_-} - e^{-\lambda_+}) \\ 1 + \frac{e^{-\lambda_+}\lambda_- - e^{-\lambda_-}\lambda_+}{\lambda_+ - \lambda_-}, \end{bmatrix} \tag{A.13}$$

and taking the second row specifically for the excited $5d$ state results in

$$n_2(t) = \frac{\sigma_{12}\phi''(e^{-\lambda_-} - e^{-\lambda_+})}{\sqrt{(\sigma_{12}\phi'' + \sigma_{23}\phi'' + w_{21}t)^2 - 4\sigma_{12}\sigma_{23}\phi''^2}}. \tag{A.14}$$

As before, the symbol ϕ'' is the cumulative integral of the photon flux rate (*i.e.*, the integral of the laser pulse profile) and is defined as

$$\phi''(t) = \int_0^t \dot{\phi}''(t')\, dt'. \tag{A.15}$$